Polymer Journal (2024) 56:379–389
https://doi.org/10.1038/s41428-023-00876-4

ORIGINAL ARTICLE

Photooxidative degradation and fragmentation behaviors of oriented isotactic polypropylene

Yingjun An[1] · Tomoko Kajiwara[1] · Adchara Padermshoke[1] · Thinh Van Nguyen[1] · Sinan Feng[1] · Hiroyasu Masunaga[2] · Yutaka Kobayashi[3] · Hiroshi Ito[3,4] · Sono Sasaki[5,6,7] · Atsuhiko Isobe[8] · Atsushi Takahara[1]

Received: 3 November 2023 / Revised: 10 December 2023 / Accepted: 11 December 2023 / Published online: 25 January 2024

Abstract

The photooxidative degradation and fragmentation behaviors of isotactic polypropylene (*it*PP) were simulated in laboratory after various postconditions, such as quenching, gradual cooling and drawing, using an artificial weathering machine and a blender. The crystallinity of the *it*PP films and orientation of the molecular chains play important roles in the photooxidation of the *it*PP films. Compared to quenched *it*PP films with the same ultraviolet (UV) exposure time, highly oriented *it*PP films and gradually cooled *it*PP films with higher crystallinity exhibited a lower rate of photooxidative degradation. To clarify the photooxidative degradation mechanism, the surface morphology, chemical structure, and microstructure of the UV-exposed *it*PP films were investigated using scanning electron microscopy, infrared spectroscopy, differential scanning calorimetry, and wide- and small-angle X-ray scattering. Photooxidative degradation was inhibited as the orientation degree of the *it*PP film increased. These results indicate that photooxidation likely occurs in the amorphous phase of *it*PP. Oriented molecular chains effectively slowed the photooxidative degradation of the *it*PP films. The artificial fragmentation test of UV-exposed *it*PP films showed that *it*PP films with lower crystallinity and orientation degrees were crushed into microplastics that were much smaller in size than those with higher crystallinity or orientation degrees.

Introduction

Plastics with desirable physicochemical properties and cost effectiveness are widely used in several fields, such as packaging, building and construction, automotive, and electronic devices [1, 2]. Large amounts of plastic products are released into the market annually, contributing to a modern world. From 1950 to 2015, the total amount of plastic products produced was 8300 million tons [1]. The widespread use of plastic products has negative impacts on the environment [3]. Large quantities of plastics are discarded after use [1]. Nearly all discarded plastic waste, such as wrappers, plastic bags, plastic bottles, fishing gear, and food containers [4], is emitted into the ocean [5]. Approximately 980,000 tons of plastic waste were emitted into the ocean in 2019 [6], which caused severe

Supplementary information The online version contains supplementary material available at https://doi.org/10.1038/s41428-023-00876-4.

✉ Atsushi Takahara
takahara.atsushi.150@m.kyushu-u.ac.jp

[1] Research Center for Negative Emission Technologies, Kyushu University, 744 Motooka, Nishi-ku, Fukuoka 819-0395, Japan

[2] Japan Synchrotron Radiation Research Institute, 1-1-1 Kouto, Sayo-cho, Sayo-gun, Hyogo 679-5198, Japan

[3] Research Center for GREEN Materials and Advanced Processing, Yamagata University, 4-3-16 Jonan, Yonezawa, Yamagata 992-8510, Japan

[4] Graduate School of Organic Materials Science, Yamagata University, 4-3-16 Jonan, Yonezawa, Yamagata 992-8510, Japan

[5] Department of Biobased Materials Science, Graduate School of Science and Technology, Kyoto Institute of Technology, 1 Matsugasaki Hashikami-cho, Sakyo-ku, Kyoto 606-8585, Japan

[6] Faculty of Fiber Science and Engineering, Kyoto Institute of Technology, 1 Matsugasaki Hashikami-cho, Sakyo-ku, Kyoto 606-8585, Japan

[7] RIKEN SPring-8 Center, 1-1-1 Kouto, Sayo-cho, Sayo-gun, Hyogo 679-5148, Japan

[8] Research Institute for Applied Mechanics, Kyushu University, 6-1 Kasuga-Koen, Kasuga 816-8580, Japan

environmental problems. Some of these waste plastics pose a threat of entanglement or ingestion by countless marine animals [7–10]. In 2013, the plastic waste mass in the global ocean reached 268,950 tons [11]. In total, 5.25 trillion plastic particles float on the ocean surface. In 2019, the amount of mismanaged plastic reached 61.8 million tons. However, once plastics are released into the environment, photooxidation and thermal oxidation induced by sunlight and oxygen occur on the surfaces of most plastics over time. In particular, mismanaged plastics floating in the ocean are fragmented into particles with sizes ranging from several millimeters to hundreds of nanometers under exposure to sunlight, abrasion by sand/rock, and wave crushing [12]. Biodegradable polymers that can be biodegraded to carbon dioxide and water by microorganisms in sediments are promising materials for relieving mismanaged plastic pollution [7, 13]. However, most plastics cannot be degraded by microorganisms in sediments and marine environments; instead, they fragment into particles and persist for extremely long periods in the environment. The plastic particles are classified by their size as macroplastics (>2.5 cm), mesoplastics (5 mm–2.5 cm), microplastics (MPs; 1 μm–5 mm), or nanoplastics (<1 μm) [14, 15]. In 2019, the macro- and microplastics in the ocean surface layer were 1.13 million and ~560,200 tons, respectively [16]. Plastic particles have several negative effects on marine organisms and humans [7, 9]. To eliminate plastic pollution, particularly the number of microplastics in the environment, the degradation and fragmentation behaviors of plastics must be determined.

Polyolefins are among the most common types of plastic. In 2015, the global production of high-density polyethylene (HDPE), low-density PE (LDPE), linear low-density PE (LLDPE), and polypropylene (PP) was 243 million tons. Thus, polyolefins are a major source of microplastic pollution [1]. Therefore, the degradation behavior of polyolefins must be determined. However, tracking the degradation of waste plastics in the natural environment is challenging. Researchers have attempted to simulate the photooxidative degradation of polyolefins in the laboratory using artificial weathering or accelerated ultraviolet (UV) exposure tests. In our previous study, we investigated the photooxidative degradation of polyolefins containing oxo-biodegradable additives [17]. The photooxidative degradation of polyolefins is promoted by oxo-biodegradable additives. The overall degradation rates of the polymers were in the order of *it*PP > LDPE > LLDPE > HDPE. Men et al. [18] studied the environmental stress cracking (ESC) of polyethylene pipes. Nakatani et al. [19] studied the degradation and fragmentation behaviors of PP and polystyrene (PS) in water. The PP microplastic production rate is much greater than that of PS owing to the crystallizability of PP. Liu et al. [20] investigated the effect of an annealing-induced microstructure on the photooxidative degradation behavior of *it*PP. The photooxidation rate was reduced by annealing the *it*PP films. Wu et al. [21] tested the photooxidative degradation behavior of *it*PP with different crystalline morphologies. They claimed that an *it*PP film with a nodular morphology exhibited improved photooxidation stability compared to that of lamellar and spherulitic structures owing to the lower O_2 diffusivity. Liu et al. investigated the photooxidation behavior of HDPE subjected to uniaxial tensile stress at various temperatures, tensile stress levels, and durations [22]. The orientation of the molecular chain plays an important role in the photooxidative degradation of HDPE. The characterization of real ocean MPs is also important for clarifying the degradation and fragmentation behaviors of plastics. On the basis of our previous research, we established advanced characterization methods for ocean MPs on the basis of polymer science [23, 24].

In this study, the effects of the crystalline structure and molecular orientation on the photooxidative degradation and fragmentation behaviors of *it*PP were investigated using quenched, gradually cooled, and uniaxially oriented *it*PP films. The photooxidative degradation of the *it*PP films was simulated by exposing the samples to UV light using an artificial weathering chamber, whereas the fragmentation behavior was studied by artificially crushing the UV-exposed *it*PP films in water using a blender. The thermal properties and chemical structures of the UV-exposed *it*PP films were investigated using differential scanning calorimetry (DSC) and Fourier transform infrared (FTIR) spectroscopy. The surface morphologies of the UV-exposed *it*PP films and artificially generated fragments were observed using scanning electron microscopy (SEM) and laser microscopy. Small- and wide-angle X-ray scattering (SAXS and WAXS, respectively) were employed to reveal the microstructures of artificially generated *it*PP fragments and real ocean PP microplastics.

Experimental section

Preparation of polypropylene films

*it*PP (MFR = 3 g/10 min) was supplied by Prime Polymer Co., Ltd. Nonoriented *it*PP films were prepared by hot pressing between steel plates with a 0.2 mm-thick spacer of tetrafluoroethylene. *it*PP pellets were melted at 210 °C for 3 min and compression-molded using a hot press machine at 6 MPa for 2 min. Quenched *it*PP films were prepared by direct cooling at 20 °C for 2 min at 6 MPa using a press machine (MP-WC, Yamato Scientific Co., Ltd.). The gradually cooled samples were cooled from a melting state to room temperature over 8 h (MP-WNH, Yamato Scientific Co., Ltd.). The sample temperature against time is shown in Fig. S1. Uniaxial-oriented *it*PP films were prepared using a

film stretcher (Toyo Seiki Seisaku-so, Ltd., EX10-S6). First, an *it*PP film with dimensions of 90 mm × 90 mm × 0.5 mm was prepared by compression at 210 °C for 4 min, hot pressing at 10 MPa for 2 min, and quenching at 20 °C for 2 min. Then, both sides of the film were clamped by gripping in a hot chamber at 158 °C. Stretching was performed in constrained uniaxial mode. The sample was stretched at 100 mm min^{-1} until the draw ratio reached two or four. After stretching, the films were immediately air-cooled to room temperature and removed from the chamber.

Ultraviolet exposure test

A weathering test chamber (Xe-1, Q-SUN, Q-LAB Co., Ltd.) with a xenon lamp was used to investigate the photooxidation behavior of the *it*PP films. Pressed and oriented *it*PP films were exposed to UV irradiation of 125 W m^{-2} ($\lambda = 300$–400 nm) and a black panel temperature of 63 °C for up to 4 w. The total UV irradiation in the accelerated UV exposure experiment was 302.4 MJ m^{-2}, which is equal to 1 y of UV exposure in Choshi, Japan [7].

Artificial fragmentation test

The fragmentation behavior of the UV-exposed *it*PP films was studied using a blender (X-TREME, Waring Commercial, Inc.). The UV-exposed *it*PP films were vacuum-dried at 40 °C overnight and weighed before fragmentation testing. The UV-exposed *it*PP films (~80 mg) were artificially crushed in 175 mL of deionized water at a blending speed of 1400 rpm for 3 min. The fragments and suspension were separated by 300 and 100 μm sieves and 10 μm filter paper. The generated fragments were dried at 40 °C for 24 h in a vacuum oven. The weights of fragments with sizes >300, 300–100, and 100–10 μm were measured using an analytical balance (XP105DRV, METTLER TOLEDO).

Characterization

The mechanical properties of the *it*PP films were studied using a tensile tester (RTI-1225, TENSILON) at a strain rate of 100% min^{-1}. The Young's modulus (E), strength at break (σ_b), and elongation at break (ε_b) values of the *it*PP films were the average of at least four measurements.

The surface morphologies of the UV-exposed *it*PP films were observed using SEM (JCM-7000, JEOL, Japan) at an accelerating voltage of 5 kV. The generated fragments were observed using a laser microscope (VK-X260, Keyence, Japan).

The IR spectra of the *it*PP films were collected using a VERTEX 70 spectrometer (Bruker) equipped with a mercury cadmium telluride (MCT) detector. A Seagull accessory (Harrick Scientific Products, Inc.) with a Ge hemispherical crystal was used for attenuated total reflection (ATR) IR measurements at a fixed incident angle of 30°. All the spectra were collected from 4000 to 675 cm^{-1} with a resolution of 4 cm^{-1}. Signals were obtained by averaging 64 scans.

DSC was used to investigate the thermal properties of the *it*PP films. Measurements were performed using a DSCvesta (Rigaku, Japan) under a nitrogen atmosphere at a heating rate of 10 °C min^{-1}. The degree of crystallinity (χ_c) was calculated from the heat of fusion at the melting point of the polymer using the following equation:

$$\chi_c{}^{DSC}\,(\%) = \frac{\Delta H_m}{\Delta H_m^\circ} \times 100\%$$

where ΔH_m denotes the heat of fusion of the *it*PP films. ΔH_m° denotes the heat of fusion of the purely crystalline forms of the polymers, corresponding to 207.1 J g^{-1} for *it*PP [25, 26].

Synchrotron radiation X-ray scattering (WAXS/SAXS) experiments were performed at the BL38B1 beamline of SPring-8 (RIKEN). The X-ray wavelength (λ) was set at 0.08 nm for WAXS and 0.1 nm for SAXS. The sample-to-detector distances were ~0.28 and 2.5 m for WAXS and SAXS, respectively. Measurements were performed in transmission geometry at room temperature with an exposure time of 10 s for each sample. WAXS and SAXS data were collected online using a 2D detector (PILATUS3X 2 M). For calibration, cerium oxide and silver behenate were used as standard samples for WAXS and SAXS, respectively. The crystallinity (χ_c) was calculated from the scattering intensity of the crystal and amorphous components I_c and I_a in the WAXS profiles using the following equation:

$$\chi_c{}^{WAXS}\,(\%) = \frac{I_c}{I_c + I_a} \times 100\%$$

where I_c and I_a were evaluated by peak decomposition from 1D WAXS profiles [27].

The crystallite size (D_{hkl}) of *it*PP samples with different UV exposure times was calculated using the Scherrer equation [28] as follows:

$$D_{hkl} = K\lambda/(\Delta\beta\cos\theta)$$

where K is the crystallite shape factor ($K = 0.89$), λ is the X-ray wavelength, $\Delta\beta$ is the half-peak width of the corresponding diffraction peak, and θ is the Bragg angle of the diffraction peak [29].

A one-dimensional electron-density correlation function, $K(z)$, for the ideal one-dimensional crystal-amorphous two-phase model [30] was employed to analyze the lamellar thickness and length of the lamellar stacking structure of the *it*PP films.

$$K(z) = \int I(q)q^2\cos(qz)\mathrm{d}q \Big/ \int I(q)q^2\mathrm{d}q$$

where $I(q)$ is the scattering intensity distribution obtained along the meridional direction (Fig. S3) and z is the real-

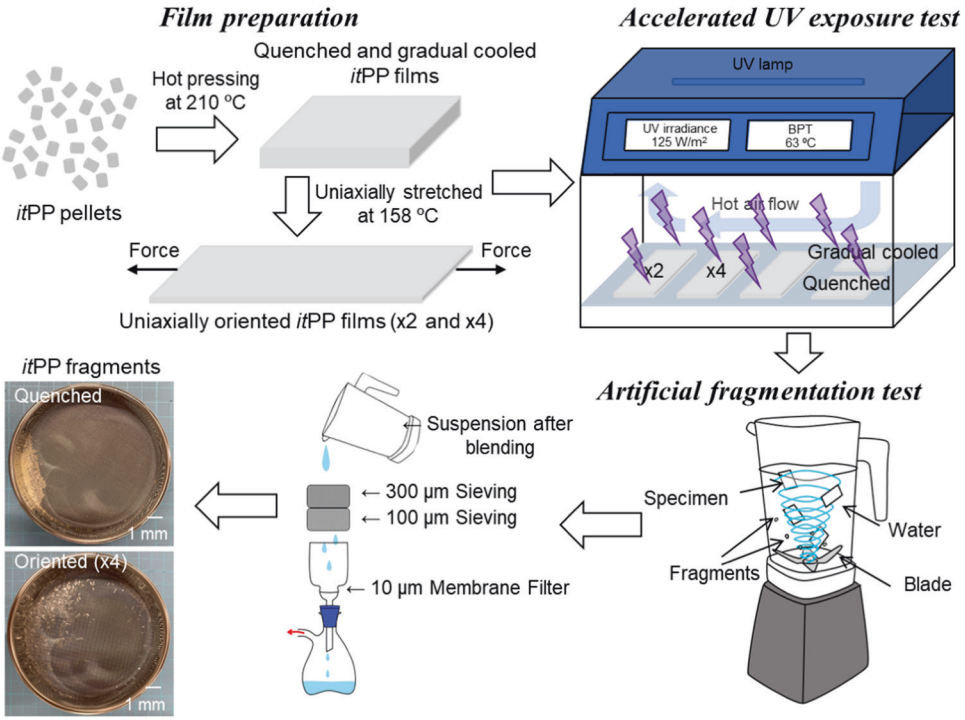

Fig. 1 Schematic of the *it*PP film preparation, UV exposure test, and artificial fragmentation test

space length parameter in the longitudinal direction. The thicknesses of the amorphous layers (d_a) were determined by identifying the intersection of the longest tangential line on the $K(z)$ profile within a specific z region. This intersection was made with a horizontal line extending from the top of the first negative peak in the profile to the z-axis. The long period of the lamellar stacking structure (L_p) was at the top of the first positive peak in the $K(z)$ profile. The lamellar thickness can be calculated by the relation $d_c = L_p - d_a$.

q is denoted here as follows:

$$q = 4\pi \sin(\theta)/\lambda$$

where 2θ and λ are the scattering angle and wavelength of the X-ray, respectively.

The orientation function (f_{040}) in the 040 direction was estimated using the azimuthal angle intensity profiles of the WAXS and the following equation [29, 31]:

$$f_{040} = (1/2)\left(3\left\langle \cos^2\phi_{040}\right\rangle - 1\right)$$

where

$$\left\langle \cos^2\phi_{040}\right\rangle = \int_0^{\pi/2} I(\phi)\sin\phi\cos^2\phi \mathrm{d}\phi \Big/ \int_0^{\pi/2} I(\phi)\sin\phi \mathrm{d}\phi$$

where ϕ is the azimuthal angle of the arc profile (Fig. S4). For the perfectly oriented and unoriented samples, f_{040} was 1 and 0, respectively.

Results and discussion

Properties of *it*PP films

Figure 1 shows the sample preparation, UV exposure, and fragmentation test of the *it*PP films. The structural information for the pressed and uniaxially oriented *it*PP films is shown in Table 1. The thermal properties of the pressed and oriented *it*PP films were evaluated using DSC (Fig. S2a). The quenched *it*PP film exhibited the lowest melting temperature ($T_{m,onset}$). The gradually cooled and uniaxially oriented *it*PP film had a higher $T_{m,onset}$ and crystallinity (χ_c) than the quenched film owing to its larger crystalline size (Table 3) and lamellar thickness (d_c). The thickness of the *it*PP films decreased with increasing draw ratio. The orientation function (f_{040}) of the uniaxially oriented film increased with the draw ratio and was 0.379 and 0.477 for the x2 and x4 elongated *it*PP films, respectively.

The lamellar thickness and length of the lamellar stacking structure of the pressed and uniaxially oriented *it*PP films were analyzed using a one-dimensional electron–density correlation function. Figure 2 shows the $K(z)$ values obtained from the $I(q)\ q^2$ values measured for the *it*PP films and the one-dimensional crystal-amorphous model, where d_c is the lamellar thickness, L_p is the long period, $\eta(z)$ is the electron density in the one-dimensional two-phase model, and $\Delta\eta$ is the difference in the electron density between the lamella and the amorphous material. The L_p and d_c values of the *it*PP films are listed in Table 1. Greater L_p and d_c values were obtained for the gradually cooled film compared to the

Table 1 Structural information of pressed and uniaxially oriented *it*PP films

*it*PP films	Thickness (μm)	$T_{m,onset}$ (°C)	χ_c (%)[a]	χ_c (%)[b]	f_{040}	L_p (nm)	d_c (nm)
Quenched	207.3 ± 9.0	151.3	41.8	54.5	0	10.3	7.6
Gradually cooled	286.6 ± 9.8	155.3	55.2	76.3	0	16.9	13.4
x2 elongated	148.3 ± 14.2	159.8	56.0	74.1	0.379	24.4	21.2
x4 elongated	112.3 ± 16.5	162.4	60.2	76.4	0.477	25.3	22.0

[a]DSC, [b]WAXS

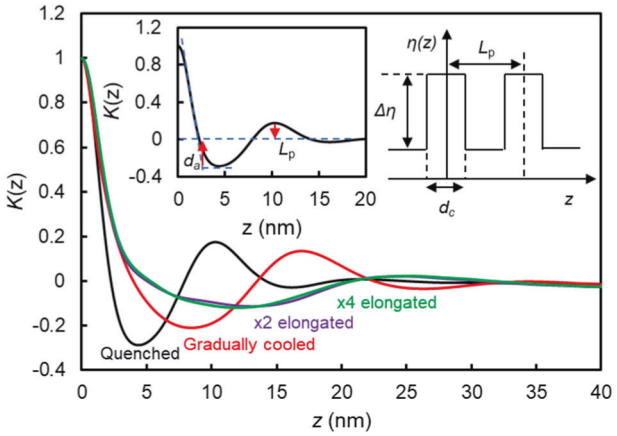

Fig. 2 One-dimensional electron-density correlation function *K(z)* evaluated for the initial *it*PP films based on the ideal one-dimensional lamella-amorphous two-phase model (the schematic for the determination of long spacing period, L_p, and lamellar thickness, d_c, electron density, $\eta(z)$, and electron density difference between a lamella and amorphous, $\Delta\eta$, are shown in the inserted figure)

quenched *it*PP film. The significant increase in lamellar thickness is attributed to the melting of imperfect and small crystallites and the subsequent recrystallization of the original thin lamellae. This increase in d_c is attributed to an increase in L_p. The L_p and d_c values of the uniaxially oriented *it*PP further increased, possibly because of the highly oriented crystalline and amorphous molecular chains. Furthermore, the pressed and uniaxially oriented *it*PP films exhibited different $\Delta\eta$ values, following the order quenched > gradually cooled > x2 ≈ x4, suggesting that the difference between the crystalline and amorphous phases in highly oriented films is smaller than that in pressed *it*PP films. In oriented films, highly oriented molecular chains form a rigid amorphous phase, which affects the physical properties of the resulting *it*PP films, such as their mechanical properties and oxygen permeability.

The mechanical properties of the quenched and x4 uniaxially elongated (parallel and perpendicular to the elongated direction) *it*PP films were measured via tensile testing. Table 2 lists the Young's modulus (E), strength at break (σ_b), and elongation at break (ε_b) of the quenched and x4 elongated *it*PP films. The Young's modulus (E) of the quenched and x4 elongated (parallel) *it*PP films were 554.7 and 1556.4 MPa, respectively. The strength at break (σ_b) was 42.2 and 134.4 MPa for the quenched and x4 elongated

Table 2 Mechanical properties of quenched and x4 elongated *it*PP films

*it*PP films	E (MPa)	ε (%)	σ (MPa)
Quenched	554.7 ± 11.2	1332.1 ± 125.0	42.2 ± 5.1
x4[a]	1556.4 ± 121.8	84.0 ± 8.6	134.4 ± 17.2
x4[b]	1423.2 ± 71.5	7.5 ± 1.5	29.6 ± 1.8

[a]Parallel to the elongation direction, [b]perpendicular to the elongation direction

*it*PP films, respectively. The E and σ of the *it*PP films increased with increasing drawing ratio owing to the orientation of the molecular chains in the *it*PP films. However, uniaxially oriented *it*PP films exhibit anisotropic mechanical properties parallel and perpendicular to the elongation direction [32, 33]. E, σ_b, and ε_b of the *it*PP films, which are perpendicular to the elongation direction, are 1423.2 MPa, 29.6 MPa, and 7.5%, respectively. For the x4 uniaxially elongated *it*PP films, both σ_b and ε_b in the uniaxially elongated direction are greater than those in the perpendicular direction.

Surface morphologies of *it*PP films after UV exposure

After 4 week of UV exposure, the surface morphologies of the pressed and uniaxially oriented *it*PP films were observed via SEM. Surface deterioration was observed on the *it*PP films after UV exposure. As shown in Fig. 3, large-scale cracks were clearly observed on the surfaces of the quenched and gradually cooled *it*PP films. Compared to the gradually cooled film, the quenched film generated significantly denser cracks, suggesting that the crack-formation behavior induced by UV exposure was affected by the crystalline and spherulite structures in the *it*PP films. Crack generation in quenched *it*PP films with lower χ_c and smaller spherulite sizes is faster than that in gradually cooled *it*PP films [34]. Cracks were also observed on the uniaxially oriented *it*PP films. Notably, the cracks that formed on the oriented *it*PP films differed from those that formed on the pressed films. The direction of the cracks on the pressed film was isotropic, whereas the cracks were parallel to the oriented direction of the uniaxially oriented *it*PP films. In the pressed *it*PP films, the crystalline and amorphous molecular chains were oriented randomly, and

photooxidation occurred equally in all directions in the pressed films after the UV exposure test. The crystalline and amorphous phases were oriented parallel to the elongation direction in the uniaxially oriented *it*PP films. The molecular chains in the transverse direction are less oriented and are photooxidized more easily than those oriented amorphously in the longitudinal direction (orientation direction). Consequently, the uniaxially oriented *it*PP films generated cracks in the direction of orientation [35]. Furthermore, the number of cracks on the oriented *it*PP films decreased with increasing draw ratio. After 4 w of UV exposure, clear cracks parallel to the orientation direction were observed on the x2 elongated *it*PP film. The number of cracks on the surface of the x4 elongated film was less than that on the surface of the x2 elongated *it*PP film. Figure S5 shows SEM images of the *it*PP films after UV exposure for 1, 2, 3, and 4 w. Cracks were generated in the pressed and oriented films with a lower degree of orientation after UV exposure for 1 week. The number of cracks gradually increased with increasing UV irradiation. Cracks were observed on the surface of the x4 elongated *it*PP films until the films were exposed to UV light for 3 w. The formation of cracks was due to photooxidation of the polymer membrane. The different crack-formation behaviors of the pressed and uniaxially oriented *it*PP films suggest that the crystalline aggregation state and molecular chain orientation are crucial for the degradation of *it*PP, inhibiting the photooxidative degradation of *it*PP films. The generation of cracks on the UV-exposed *it*PP film surfaces may have resulted from chain scission during photooxidation. White et al. [36] reported that chain scission and crosslinking occurred in polyolefins under UV exposure. Upon UV exposure, radicals are formed, initiating a subsequent photooxidation process that generates products such as ketones, esters/aldehydes, lactones, and carboxylic acids. This photooxidation results in a decrease in molecular weight, leading to the formation of cracks on the surface of the *it*PP films. As the photooxidation reaction progresses on the film surface, oxygen is rapidly consumed. Consequently, crosslinking becomes dominant due to the lower oxygen concentration, leading to gel formation [37].

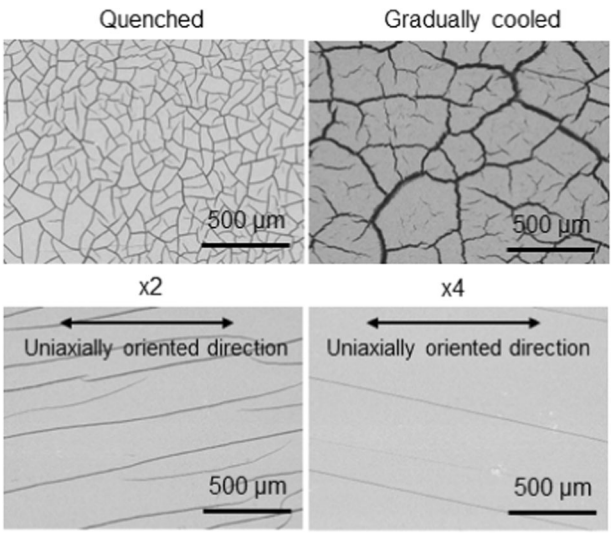

Fig. 3 SEM images of quenched, gradually cooled and uniaxially oriented *it*PP films after 4 w of accelerated UV exposure test

Thermal properties of *it*PP films after the UV exposure test

The thermal properties of the *it*PP films after UV exposure were measured using DSC. The dependence of the onset melting temperature ($T_{m,onset}$) and χ_c on UV irradiation is shown in Fig. 4. The $T_{m,onset}$ values of the quenched and gradually cooled *it*PP films decreased gradually with increasing UV exposure. After the *it*PP films were UV exposed for 4 w, the $T_{m,onset}$ values of the quenched and gradually cooled *it*PP films decreased from 151.3 and 155.3 °C to 118.6 and 138.6 °C, respectively. The $T_{m,onset}$ of uniaxially oriented *it*PP films slightly decreased after the UV exposure test, from 159.8 and 162.4 °C to 159 and

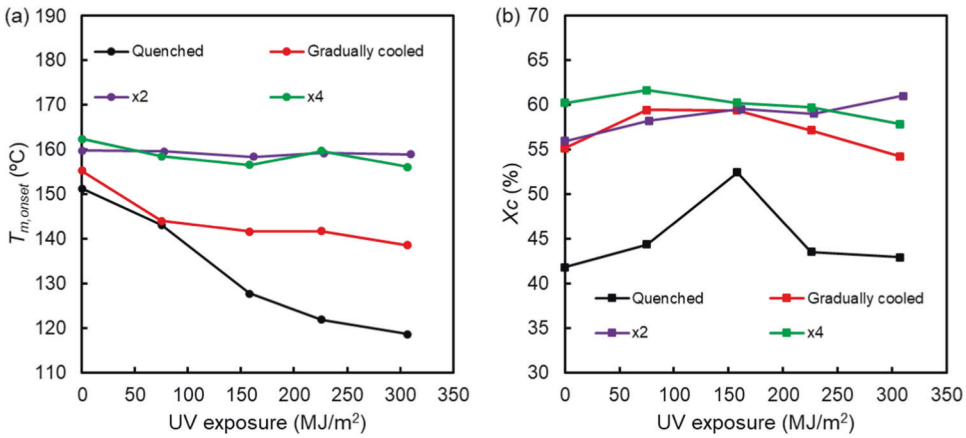

Fig. 4 Effect of UV exposure on thermal properties of *it*PP films. (**a**) Onset melting temperature, (**b**) crystallinity of *it*PP films

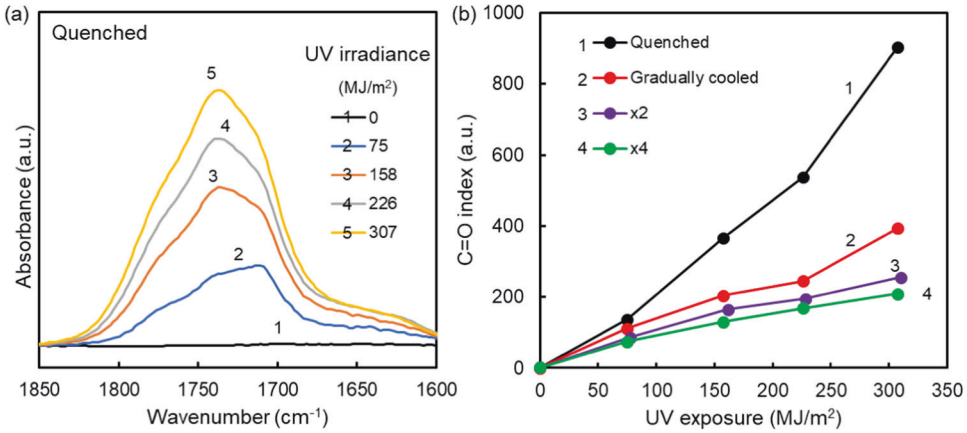

Fig. 5 (**a**) Normalized ATR FTIR spectra of quenched *it*PP films before and after UV exposure test. (**b**) Comparison of the CI of pressed and oriented *it*PP films as a function of UV irradiation

156.1 °C for the x2 and x4 elongated *it*PP films, respectively. The melting temperatures of the crystalline and semicrystalline polymers were proportional to the thickness of the lamellar structure [38]. The decrease in melting temperature of the *it*PP films indicated that the crystalline size decreased after the UV exposure test. Compared to the gradually cooled films, the quenched *it*PP films exhibited a faster photooxidative degradation rate. The photooxidative degradation rate of the uniaxially oriented films was slower than that of the pressed films. The crystallinity (χ_c) of the *it*PP films obtained after the UV exposure test is shown in Fig. 4b. The χ_c of the quenched *it*PP films increased with increasing exposure to UV irradiation and was the highest after 2 w of UV exposure. Then, χ_c decreased with increasing UV irradiation. For the gradually cooled *it*PP films, χ_c was the highest after 1 w of UV exposure. Then, the value gradually decreased with increasing UV irradiation. The χ_c of uniaxially oriented *it*PP films was nearly constant with increasing UV irradiation. For the pressed *it*PP films, χ_c first increased and then decreased with increasing UV irradiation. This possibly resulted from the thermal treatment of the quenched *it*PP films in the weathering machine during the first 2 w. Subsequently, the amorphous phase with flexible molecular chains and high oxygen solubility and the crystalline phase were photooxidized, the lamellar structure was destroyed, and a smaller crystallite size was generated.

Ultraviolet degradation evaluated by infrared spectroscopy

FTIR spectroscopy is a useful tool for monitoring the polymer degradation process and identifying degradation products. This approach was used to investigate the photooxidation behavior of the pressed and uniaxially oriented *it*PP films. In our previous study, the photooxidative degradation of polyolefins was studied using FTIR [17]. Carbonyl-containing products, such as ketones, esters/aldehydes, lactones, and carboxylic acids, were generated during photooxidation. The carbonyl index (CI) was used to evaluate the photooxidative degradation rate of the pressed and uniaxially oriented *it*PP films. The CI was evaluated from the generated C = O and reference C–H bands using the following equation:

$$CI = A_{C=O}/A_{Ref}$$

where $A_{C=O}$ and A_{Ref} are the integrated areas of the C = O (1840–1650 cm^{-1}) and reference C–H (1340–1315 cm^{-1}) bands, respectively. Figure 5a shows the IR spectra in the C = O stretching ($\nu_{C=O}$) regions of the quenched *it*PP films collected as a function of the integrated UV irradiation. No C = O absorption is observed in the initial *it*PP film. After UV exposure, $\nu_{C=O}$ bands appeared and considerably increased with increasing UV exposure. The CIs of the *it*PP films, calculated as a function of UV irradiation, are shown in Fig. 5b. The CI gradually increased with increasing UV irradiation in the pressed and uniaxially oriented *it*PP films. The quenched *it*PP film exhibited greater CIs than those of the gradually cooled and uniaxially oriented films and 2.3, 3.5, and 4.3 times greater than those of the gradually cooled, x2, and x4 elongated *it*PP films, respectively, after 4 w of UV exposure. The generation of carbonyl groups in the UV-exposed *it*PP films suggested that the photooxidation susceptibility of the *it*PP films was in the following order: quenched > gradually cooled > x2 > x4. The photooxidative degradation of the *it*PP films was inhibited by the oriented molecular chains.

Microstructure of *it*PP films after UV exposure

The microstructural changes in the *it*PP films before and after UV exposure were investigated using WAXS. The inhibitory effect of chain orientation on the photooxidation of *it*PP films was corroborated by the crystallite size changes in the virgin and UV-exposed pressed and

Table 3 Crystallite size of *it*PP films before and after the UV exposure test

*it*PP films	Crystallite size (nm)					
	α (110)		α (040)		α (130)	
	Initial	UV_4w	Initial	UV_4w	Initial	UV_4w
Quenched	14.5	13.6	16.9	15.8	11.8	10.7
Gradually cooled	23.6	17.1	22.3	19.3	19.1	12.7
x2 elongated	31.9	29.5	26.6	25.1	25.6	23.7
x4 elongated	29.2	27.9	23.6	22.6	23.2	22.2

uniaxially oriented *it*PP films. The 1D WAXS profiles of the pressed and uniaxially oriented *it*PP films are shown in Fig. S8. Curve fitting of the 1D WAXS profiles was conducted using Origin 2023 software; Gaussian functions were chosen to fit the amorphous halo, and Gaussian/Lorentz profiles were used for the scattering peaks. Table 3 lists the crystallite sizes of the *it*PP films before and after UV exposure. The crystallite sizes of the gradually cooled and uniaxially oriented films were much larger than those of the quenched film, corresponding to a higher melting temperature. After a 4 w UV exposure test, the crystallite size in the pressed *it*PP films decreased, suggesting that the crystallite structure of the pressed *it*PP films was destroyed during photooxidative degradation. However, the crystallite size of the uniaxially oriented *it*PP films remained nearly constant after UV exposure. The changes in the crystallite size of the *it*PP films after UV exposure corresponded with the DSC results.

Fragmentation behaviors of the UV-exposed *it*PP films

The UV-exposed pressed and uniaxially oriented *it*PP films were artificially fragmented using a blender. The generated fragments were observed under a laser microscope. Figure 6 shows the fragments generated from the UV-exposed quenched, gradually cooled, x2 elongated, and x4 elongated *it*PP films. Among the pressed *it*PP films, the quenched film generated significantly smaller particles than the gradually cooled film. The particle sizes generated from the UV-exposed quenched and gradually cooled *it*PP films ranged from 96 to 1145 μm and 300 to 1470 μm, respectively. The particles generated from the UV-exposed uniaxially oriented *it*PP films were significantly larger than those generated from the pressed films. Therefore, the photooxidation rate in the *it*PP films was decreased by the oriented molecular chains. Notably, the shape of the generated particles was anisotropic, and the long axis was the same as the chain orientation direction.

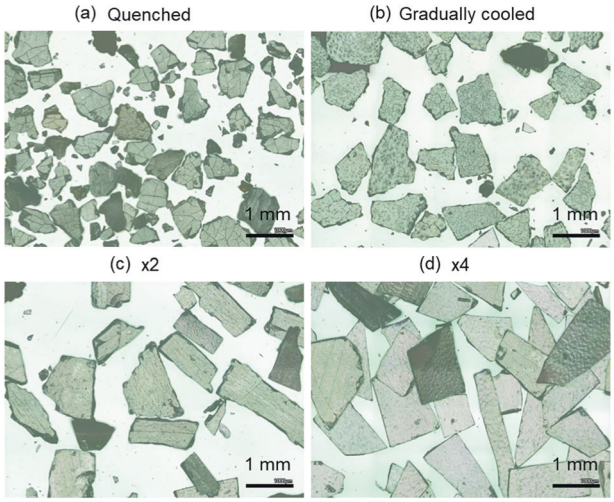

Fig. 6 Laser microscope images of *it*PP fragments. (**a**) Quenched, (**b**) gradually cooled, (**c**) x2 elongated, (**d**) x4 elongated *it*PP

Comparison of UV-exposed *it*PP MPs and real ocean MPs

Figure 7 shows laser microscopy images of four real ocean MPs collected from the Tsushima Strait [39]. The ocean MPs collection method is described in the SI. The oceanic MPs were named as W-9, W-12, W-22, and W-31. The shape of ocean MPs is anisotropic and similar to that of fragments generated from UV-exposed uniaxially oriented *it*PP films. Cracks were observed on the surface of the W-12 ocean MPs. Furthermore, the direction of the cracks was primarily along the long axis. Microbes were also observed on the surface of ocean MPs (Fig. 7e, f). The types of oceanic MPs were identified using WAXS (Fig. 8). All four ocean MPs were PP fragments. Diffraction peaks, such as the (110), (040), (130), (111) and (13$\bar{1}$)/(041) planes of the α crystal form of *it*PP, were observed. Importantly, all four ocean MPs were oriented, which indicates that most ocean PP MPs were oriented.

Conclusions

Pressed and uniaxially oriented *it*PP films were prepared, and their photooxidative degradation and fragmentation behaviors were studied in the laboratory using an artificial weathering machine and a blender. The oriented molecular chains improved the mechanical properties of the *it*PP films. After UV exposure, chain scissions and interactions occurred in the *it*PP films. Random cracks were formed on the surfaces of the quenched and gradually cooled films. The direction of the cracks on the uniaxially oriented *it*PP films was anisotropic and parallel to the chain-oriented direction. Furthermore, the number of cracks decreased in

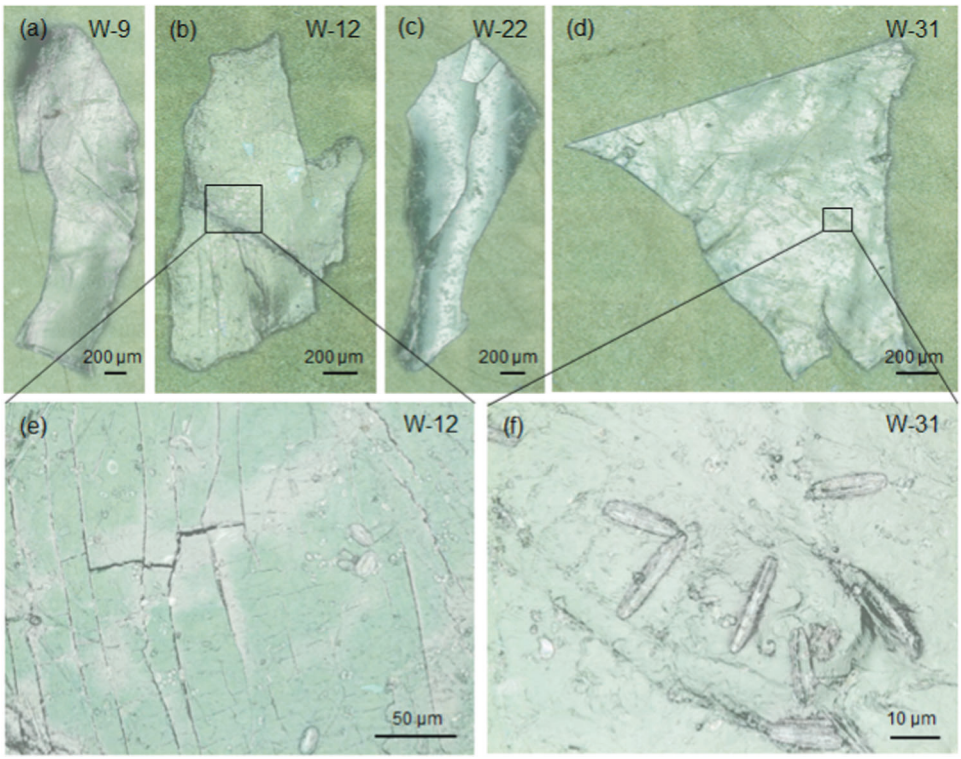

Fig. 7 Laser microscope images of ocean PP microplastics

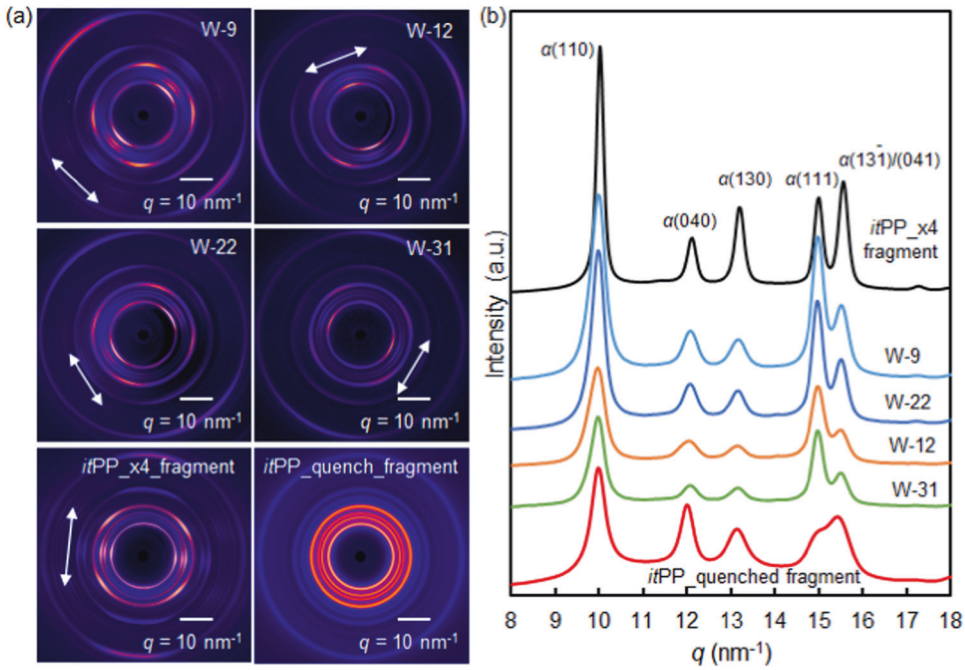

Fig. 8 2D WAXS patterns (**a**) and 1D profiles (circularly integrating) (**b**) of ocean PP microplastics (W-i corresponds to images in Figure 7) and artificial UV-exposed *it*PP fragments

the highly oriented *it*PP films. Photooxidation occurred in the UV-exposed *it*PP films, as confirmed by FTIR spectroscopy. The photooxidation susceptibility of the *it*PP films followed the order of quenched > gradually cooled > x2 elongated > x4 elongated. Compared to the pressed films, the uniaxially oriented *it*PP films exhibited more stable thermal properties. Compared to the gradually cooled and uniaxially oriented *it*PP films, the quenched *it*PP films generated much smaller particles, as suggested by the fragmentation test of the UV-exposed *it*PP films. The photooxidative degradation and fragmentation of the *it*PP films were inhibited by the oriented molecular chains. Observations of ocean MPs suggest that most ocean PP MPs are oriented. Ocean PP MPs exhibited shapes and

structures similar to those of the fragments generated from UV-exposed uniaxially oriented *it*PP films.

Acknowledgements This work is based on results obtained from a project, PNP18016, commissioned by the New Energy and Industrial Technology Development Organization (NEDO). The authors also acknowledge the financial support of the JSPS Grant-in- for Scientific Research (Grant No. 26248053). WAXS and SAXS data were obtained at the BL38B1 beamline of the SPring-8 synchrotron facility in Japan with the approval of RIKEN.

Compliance with ethical standards

Conflict of interest The authors declare no competing interests.

References

1. Geyer R, Jambeck J, Law K. Production, use, and fate of all plastics ever made. Sci Adv. 2017;3:e1700782.
2. Geyer R Chapter 2 - Production, use, and fate of synthetic polymers. In: Letcher TM, editors. Plastic waste and recycling. Academic; 2020. p. 13–32.
3. Koelmans AA, Redondo-Hasselerharm PE, Nor NHM, de Ruijter VN, Mintenig SM, Kooi M. Risk assessment of microplastic particles. Nat Rev Mater. 2022;7:138–52.
4. Morales-Caselles C, Viejo J, Martí E, González-Fernández D, Pragnell-Raasch H, González-Gordillo JI, et al. An inshore–offshore sorting system revealed from global classification of ocean litter. Nat Sustain. 2021;4:484–93.
5. Jambeck J, Geyer R, Wilcox C, Siegler T, Perryman M, Andrady A, et al. Plastic waste inputs from land into the ocean. Science. 2015;347:768–71.
6. Meijer L, Emmerik T, Ent R, Schmidt C, Lebreton L. More than 1000 rivers account for 80% of global riverine plastic emissions into the ocean. Sci Adv. 2021;7:eaaz5803.
7. An Y, Kajiwara T, Padermshoke A, Nguyen T, Feng S, Mokudai H, et al. Environmental Degradation of nylon, poly(ethylene terephthalate) (PET), and poly(vinylidene fluoride) (PVDF) fishing line fibers. ACS Appl Polym Mater. 2023;5:4427–36.
8. Clark BL, Carneiro APB, Pearmain EJ, Rouyer MM, Clay TA, Cowger W, et al. Global assessment of marine plastic exposure risk for oceanic birds. Nat Commun. 2023;14:3665.
9. EFSA CONTAM Panel (EFSA Panel on Contaminants in the Food Chain). Statement on the presence of microplastics and nanoplastics in food, with particular focus on seafood. EFSA J. 2016;14:450.
10. Lim X. Microplastics are everywhere - but are they harmful? Nature. 2021;593:22–5.
11. Eriksen M, Lebreton LCM, Carson HS, Thiel M, Moore CJ, Borerro JC, et al. Plastic pollution in the world's oceans: More than 5 trillion plastic pieces weighing over 250,000 tons afloat at sea. PLOS ONE. 2014;9:e111913.
12. Carpenter E, Smith K. Plastics on the Sargasso sea surface. Science. 1972;175:1240.
13. Eto R, Mokudai H, Masaki T, Matsuno H, Tanaka K. Hydrolysis properties of polyglycolide fiber mats mixed with a hyperbranched polymer as a degradation promoter. Polym J. 2024;56:55–60.
14. Science to enable sustainable plastics—A white paper from the 8th Chemical Sciences and Society Summit (CS3), 2020, rsc.li/sustainableplastics-report. https://www.rsc.org/globalassets/22-newperspectives/sustainability/progressive-plastics/c19_tl_sustainability_cs3_whitepaper_a4_web_final.pdf. Accessed 29 December, 2023.
15. Law K, Narayan R. Reducing environmental plastic pollution by designing polymer materials for managed end-of-life. Nat Rev Mater. 2022;7:104–16.
16. Lebreton L, Egger M, Slat B. A global mass budget for positively buoyant macroplastic debris in the ocean. Sci Rep. 2019;9:12922.
17. Padermshoke A, Kajiwara T, An Y, Takigawa M, Nguyen T, Masunaga H, et al. Characterization of photo-oxidative degradation process of polyolefins containing oxo-biodegradable additives. Polymer. 2022;262:125455.
18. Qin Y, Litvinov V, Chassé W, Sun J, Men Y. Environmental stress cracking of polyethylene pipe: Changes in physical structures leading to failure. Polymer. 2022;252:124938.
19. Nakatani H, Ohshima Y, Uchiyama T, Motokucho S. Degradation and fragmentation behavior of polypropylene and polystyrene in water. Sci Rep. 2022;12:18501.
20. Liu Q, Liu S, Xia L, Hu P, Lv Y, Liu J, et al. Effect of annealing-induced microstructure on the photo-oxidative degradation behavior of isotactic polypropylene. Polym Degrad Stab. 2019;162:180–95.
21. Wu H, Zhao Y, Su L, Wang K, Dong X, Wang D. Markedly improved photo-oxidation stability of α form isotactic polypropylene with nodular morphology. Polym Degrad Stab. 2021;189:109595.
22. Liu Q, Yang H, Zhao J, Liu S, Xia L, Hu P, et al. Acceleratory and inhibitory effects of uniaxial tensile stress on the photo-oxidation of polyethylene: Dependence of stress, time duration and temperature. Polymer. 2018;148:316–29.
23. Kajiwara T, An Y, Padermshoke A, Kumagai A, Marubayahi H, Ikemoto Y, et al. Characterization of microplastics by advanced analytical techniques. Bunseki Kagaku. 2022;71:541–47.
24. Takahara A, Kajiwara T, An Y. Analysis of formation process of polyolefin microplastics on the basis of polymer science. Bull Coast Oceanogr. 2023;61:89–93.
25. Lima MFS, Vasconcellos MAZ, Samios D. Crystallinity changes in plastically deformed isotactic polypropylene evaluated by X-ray diffraction and differential scanning calorimetry methods. J Polym Sci B: Polym Phys. 2002;40:896–903.
26. Krevelen DW, Nijenhuis K Chapter 5 - Calorimetric properties. In Properties of polymers (Fourth Edition). Elsevier, Amsterdam; 2009. p. 109–28.
27. Weidinger A, Hermans P. On the determination of the crystalline fraction of isotactic polypropylene from X-ray diffraction. Die Makromol Chem. 1961;50:98–115.
28. Yamaji K, Haisa M. Dynamic mechanical and X-ray studies of annealed isotactic polypropylene. Jpn J Appl Phys. 1976;15:225.
29. Alexander L X-ray diffraction methods in polymer science. John Wiley, New York, 1970.
30. Strobl GR, Schneider M. Direct evaluation of the electron density correlation function of partially crystalline polymers. J Polym Sci Polym Phys Ed. 1980;18:1343–59.
31. Tashiro K Crystal Structure analysis by wide-angle X-ray diffraction method. In: Tashiro K, editors. Structural science of crystalline polymers: Basic concepts and practices. Springer Nature Singapore; 2022. p. 1–285.
32. Dhingra VJ, Spruiell JE, Clark ES. The relationship between mechanical properties and structure in rolled polypropylene. Polym Eng Sci. 1981;21:1063–71.
33. Higashida Y, Watanabe K, Kikuma T. Mechanical properties of uniaxially and biaxially rolled polymer sheets. ISIJ Int. 1991;31:655–60.
34. Ballesteros O, Stefano F, Auriemma F, Girolamo R, Scoti M, Rosa C. Evidence of nodular morphology in syndiotactic polypropylene from the quenched state. Macromolecules. 2021;54:7540–51.

35. Lu Y, Wang Y, Chen R, Zhao J, Jiang Z, Men Y. Cavitation in isotactic polypropylene at large strains during tensile deformation at elevated temperatures. Macromolecules. 2015;48:5799–806.
36. White J, Shyichuk A. Macromolecular scission and crosslinking rate changes during polyolefin photo-oxidation. Polym Degrad Stab. 2007;92:1161–8.
37. Grause G, Chien M, Inoue C. Changes during the weathering of polyolefins. Polym Degrad Stab. 2020;181:109364.
38. Maiti P, Hikosaka M, Yamada K, Toda A, Gu F. Lamellar thickening in isotactic polypropylene with high tacticity crystallized at high temperature. Macromolecules. 2000;33:9069–75.
39. Isobe A, Uchiyama-Matsumoto K, Uchida K, Tokai T. Microplastics in the Southern Ocean. Mar Pollut Bull. 2017;114:623–6.